Article

Effects of Process Parameters on the Bead Shape in the Tandem Gas Metal Arc Welding of Aluminum 5083-O Alloy

Gwang-Gook Kim [1,2], Taehoon Kang [1], Dong-Yoon Kim [1,2], Young-Min Kim [1,*], Jiyoung Yu [1,*] and Junhong Park [2]

[1] Advanced Joining & Additive Manufacturing R&D Department, Korea Institute of Industrial Technology, 156 Gaetbeol-ro, Yeonsu-gu, Incheon 21999, Republic of Korea; kimgg@kitech.re.kr (G.-G.K.); rroyy147@gmail.com (T.K.); kimdy@kitech.re.kr (D.-Y.K.)

[2] Department of Mechanical Convergence Engineering, Hanyang University, Seoul 04763, Republic of Korea; parkj@hanyang.ac.kr

* Correspondence: ymkim77@kitech.re.kr (Y.-M.K.); willow@kitech.re.kr (J.Y.)

Abstract: In gas metal arc welding (GMAW), the weld bead shape is an important factor that is directly related to the weld quality of welded joints. This study investigates the effects of process parameters, including welding speed (WS) and leading and trailing wire feed rates (WFR), on the weld bead shape, including the leg length and penetration depth, in the tandem GMAW of aluminum 5083-O alloy. An asynchronous direct current–direct current pulse tandem GMAW system and a tandem GMAW torch were designed and applied to improve welding productivity and welding quality. Response surface methodology was used to analyze the effects of the process parameters on the weld bead shape and to estimate regression models for predicting the weld bead shape. As a result of observing arc behavior using a high-speed camera, it was confirmed that the leading WFR affects the penetration depth and the trailing WFR affects the leg length. The coefficient of determination (R^2) of the regression models was 0.9414 for the leg length and 0.9924 for the penetration depth. It was also validated that the estimated models were effective in predicting the weld bead shape (leg length and penetration depth) representative of weld quality in the tandem GMAW process.

Keywords: 5xxx series aluminum alloy; tandem gas metal arc welding; tandem process parameters; response surface methodology; weld quality

1. Introduction

The application of aluminum in automotive parts is increasing to reduce vehicle weight. Various joining processes are applied to join aluminum parts [1,2]. Among the various joining processes, gas metal arc welding (GMAW) is an efficient welding process that is particularly suitable for welding metal plates. Whereas a general GMAW process uses a single arc, the tandem GMAW process used in this study comprises two independent welding machines, each with its own power source, welding torch, wire drive, and welding wire. Owing to its system characteristics, the tandem GMAW process has a higher deposition rate and welding speed than the conventional single-wire GMAW process, implying that the tandem GMAW process can improve welding productivity [3–8]. However, the welding system and arc behavior of tandem GMAW are more complex than those of conventional single-wire GMAW such that it is necessary to establish the effects of process parameters on the weld bead shape, which is directly related to weld quality, and welding quality in tandem with the GMAW process. Kolahan et al. [8] developed a model to analyze the influence of the wire feed rate (WFR), torch angle, welding speed, and nozzle-to-plate distance on the weld bead height, width, and penetration depth in the GMAW process through the design of experiments (DOEs). The fit of the model was confirmed through an analysis of variance (ANOVA). Saravanan et al. [9] optimized the strength according to the welding parameters (current, voltage, gas flow rate, torch angle, welding speed,

wire diameter, and electrode feed rate) in aluminum GMAW using the Taguchi method. Jayaganesh et al. [10] optimized the tensile strength and mass deposition rate according to the welding current, WFR, and welding speed among the GMAW parameters using the DOE. The results confirmed that the WFR and welding current are important variables. Venkadeshwaran et al. [11] derived the optimal ultimate tensile strength through an L9 orthogonal array by optimizing the welding current, voltage, and gas flow rate among the welding parameters in the GMAW of aluminum alloy. Ramarao et al. [12] optimized the welding parameters (welding current, voltage, and bevel angle) to obtain better impact strength using the Taguchi L9 orthogonal array in GMAW and proved that the current and voltage are the main factors through ANOVA. Duan et al. [13] performed GMAW on metals with narrow gaps and optimized welding parameters, such as the rotation angular velocity, rotation angular amplitude, WFR, welding speed, and sidewall stay time, to optimize the welding quality. Tham et al. [14] performed GMAW on the shape of a T-fillet joint and developed a mathematical model to predict the bead shape according to the welding parameters (welding current, welding voltage, welding speed, and wire extension). Consequently, the deviation between the predicted and actual values was less than 1.0 mm. Yu et al. [15] investigated the effects of welding current and torch position parameters, including the torch-aiming position, travel angle, and work angle, on the bead geometry in a single-lap joint GMAW. Shen et al. [16] analyzed the effect of welding parameters on the formation of gas metal arc welding—gas tungsten arc welding (GMAW–GTAW) double-arc welding and provided optimal conditions for obtaining high-quality and good forming. Rodriguez et al. [17] compared a 6.35 mm thick 6061 aluminum alloy with the GMAW process using the hybrid GTAW–GMAW and confirmed that the GTAW–GMAW promoted grain structure refinement and reduced porosity in the welded metal. In addition, the GTAW–GMAW process reduced the degradation in the heat-affected zone under the as-weld condition and increased the welding speed by 40%. Lee et al. [18] developed a model that optimizes the parameters through a Gaussian process regression model for the bead shape in a tandem flux cored arc welding process. Wu et al. [19] studied the temperature and fluid flow fields using a three-dimensional numerical model in the tandem GMAW process and investigated the resulting molten pool formation, convection, and stability. Häßler et al. [20] investigated the arc stabilization effect of filler wires using high-speed recordings and numerical calculations in a tandem GMAW process. However, research that focused on the effects of the process parameters on the weld bead shape in tandem GMAW of aluminum alloys for automotive parts is insufficient. Wu et al. [21] investigated the welding bead shape for each pulse waveform with different phase shifts by synchronizing the welding power source in the aluminum alloy tandem GMAW. Synchronous control requires additional hardware and control software.

In this study, the effects of process parameters, including welding speed (WS) and leading and trailing WFRs, on the weld bead shape, including leg length and penetration depth, in the tandem GMAW of aluminum 5083-O alloy were investigated using an asynchronous direct current–direct current (DC–DC) pulse tandem GMAW system. Response surface methodology (RSM) was used to investigate the effects of the welding parameters on the weld bead shape and to estimate regression models for predicting the weld bead shape.

2. Materials and Methods

2.1. Materials

Aluminum 5083-O alloy, used in automotive parts, such as a cowl cross bar, was used. Table 1 summarizes the chemical composition of the aluminum 5083-O alloy. The thickness of the aluminum 5083-O alloy used in this study is 1.5 and 2.5 mm. Figure 1 shows the configuration of the single-lap-joint. The workpiece was cut into dimensions of 150 mm × 150 mm, and an overlap width of 20 mm was used for the welding test.

Table 1. Chemical composition of aluminum 5083-O alloy (wt.%).

Si	Fe	Cu	Mn	Mg	Cr	Zn	Ti	Al
0.11	0.31	0.05	0.66	4.51	0.09	0.03	0.01	94.2
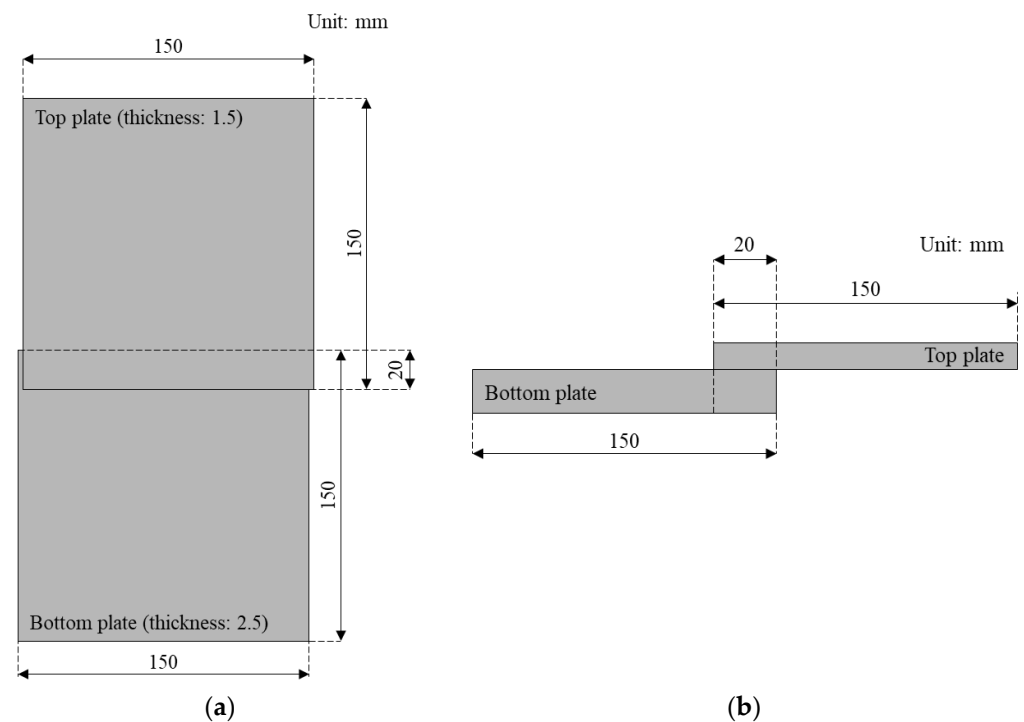
Figure 1. Schematic diagram of single-lap-joint: (**a**) top view; (**b**) side view.

2.2. Welding Equipment

A synchronous tandem GMAW system synchronizes the waveforms from the power sources of the two welding machines that have a phase difference of a certain value between the two waveforms. Additional components such as the controller and coupling module and complex control logic are required to control the two welding machines of the synchronous tandem GMAW. In contrast, an asynchronous tandem GMAW system has the advantage of being able to configure the system without additional complex components, and each welding machine of the asynchronous tandem GMAW system independently operates and outputs its own waveform. Figure 2 shows the schematic of the asynchronous tandem welding equipment used in this study, which comprises two inverter-based welding power sources: Welbee W350 (Daihen Corporation, Osaka, Japan) for the leading wire and Welbee P500L (Daihen Corporation, Osaka, Japan) for the trailing wire. The tandem control type is asynchronous, and DC pulse is selected for both leading and trailing current types. Figure 3 shows the welding current and voltage waveforms at a leading wire feed rate of 9.5 m/min and a trailing wire feed rate of 5.0 m/min. The current of the welding power source is controlled individually for the two electrodes without the hardware to control synchronization. In general, the tandem GMAW process can increase productivity such as the welding speed and high deposition rate. However, the large torch size of the tandem GMAW system may limit the applications of the tandem GMAW system because the large torch causes more interference with workpieces and jigs compared to the torch of a conventional single-wire GMAW system. To address this limitation, a tandem torch with a smaller size than the existing tandem torch was designed and fabricated in the study. The designed torch has heat resistance so that it can be used for a tandem total current of 500 A. A design process was performed to select angles and distances to prevent interference between contact tips. The outer diameter of the contact tip is 5 mm, and the distance between the wires is 7 mm. The outer diameter of the torch nozzle is 24 mm, which

is smaller than the 25 mm outer diameter of the existing single-torch nozzle. A schematic of the torch used in the test is shown in Figure 4.
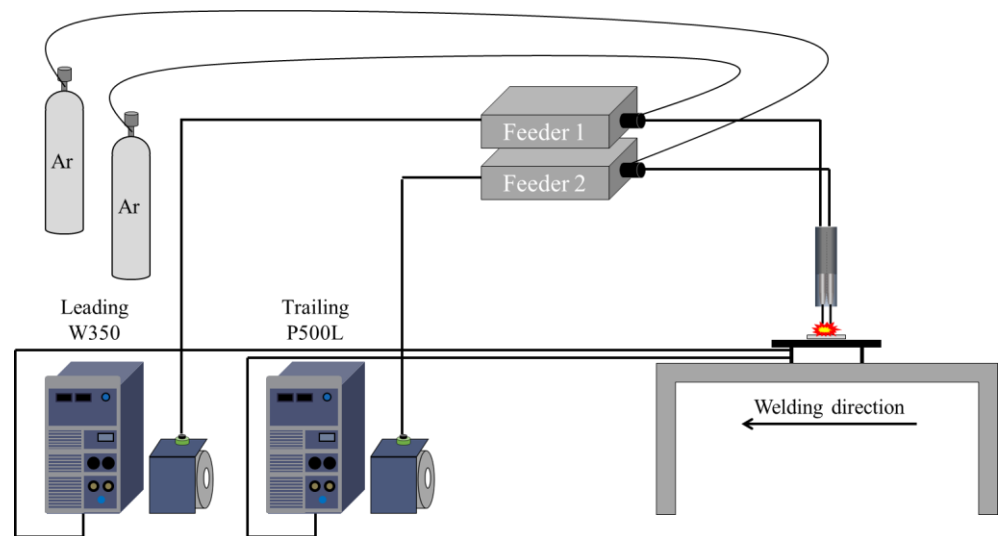

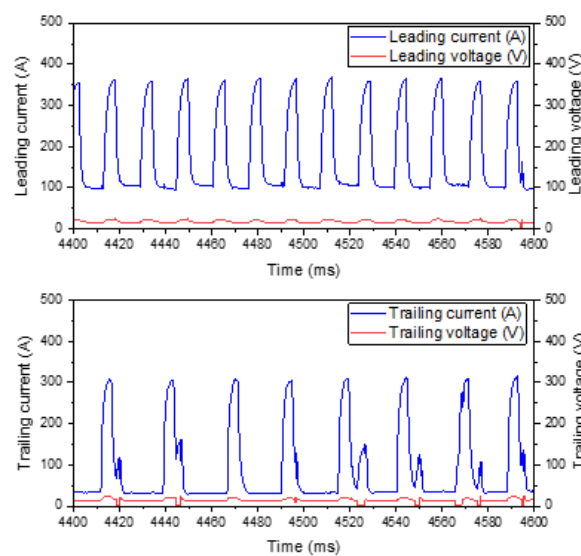**Figure 2.** Schematic diagram of welding equipment.

Figure 3. Current and voltage waveforms of the tandem gas metal arc welding system when leading WFR is 9.5 m/min and trailing WFR is 5.0 m/min.
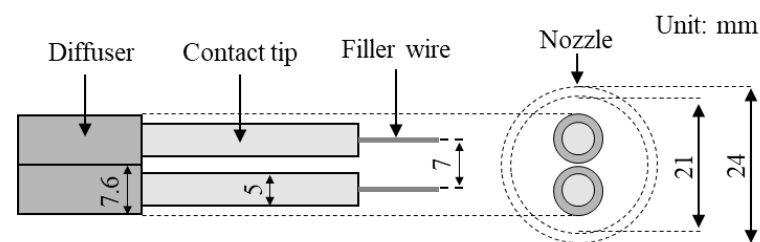

Figure 4. Schematic diagram of designed tandem welding torch.

2.3. Welding Conditions

A synchronous Table 2 lists the welding conditions. In both GMAW machines of the tandem welding system, the current type used a DC pulse for the polarity of the direct

current electrode positive. A 1.2 mm diameter ER5356 welding wire specified in AWS A5.10/A5.10M:2021 was used, and the WS was 123–157 cm/min. The work angle was 30°, and the range of WFR was 2.6–9.5 m/min. The contact tip-to-workpiece distance was set as shown in Figure 5, which is a schematic diagram of the tandem GMAW.

Table 2. Welding conditions.

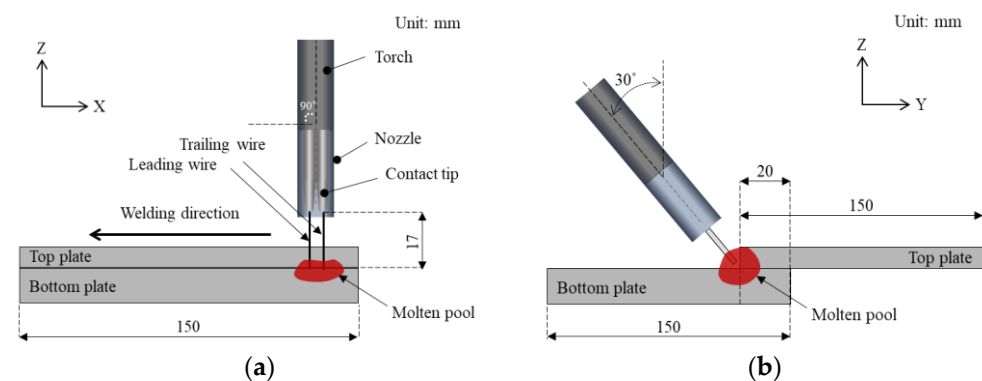| Condition	Leading Arc	Trailing Arc
Power source	Welbee P500L	Welbee W350
Current type	DC pulse (Polarity: DCEP)	
Filler wire	ER5356 (diameter: 1.2 mm)	
Wire feed rate (m/min)	2.6–9.5	
Welding speed (cm/min)	123–157	
Work angle (°)	30	
CTWD (mm)	17	
Shielding gas	Ar (15 L/min)	Ar (15 L/min)

Figure 5. Schematic diagram of the lap fillet joint shape, travel angle, and work angle for tandem gas metal arc welding: (**a**) X-Z plane; (**b**) Y-Z plane.

2.4. Analysis Method

This study investigated the effects of three welding parameters (independent variables), including WS (X_1), leading WFR (X_2), and trailing WFR (X_3), on the response variables, leg length (Y_{leg}), and penetration depth (Y_{pen}), as shown in Figure 6. Optical microscopy was used to observe the response variables. Polishing and etching were performed to measure the cross-sectional shape of the weld beads. Sodium hydroxide was used for etching. Response variables were identified using a microscope connected to image analysis software. A central composite design (CCD) and RSM were used to analyze the effects of the welding parameters. The CCD describes the relationship between the independent and response variables and estimates a second-order response surface model. CCD with three factors (X_1, X_2, and X_3 in this study) consists of three parts: eight factorial points, six center points, and eight axial points. The position α value of the axial point was determined by the number of experiments at the origin, which is the center point of the region of interest of the CCD. Because it has three parameters, the value of α is 1.682. The factor levels of the natural and design units used in the experiment are listed in Table 3. A high-speed camera was used to investigate the effects of the welding parameters on the behavior of the molten pool, and a schematic is shown in Figure 7. To acquire the image, an illumination laser with a wavelength of 808 nm was used, and 808 nm band pass filters with full width at half maximum (FWHM) values of 10 and 5 were sequentially applied to the camera. To prevent excessive exposure to strong arc light, a neutral density filter (ND filter) was used.
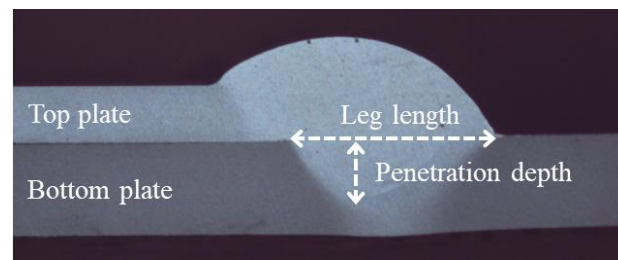
Figure 6. Schematic diagram of leg length and penetration depth.

Table 3. Factor levels in natural and design units.

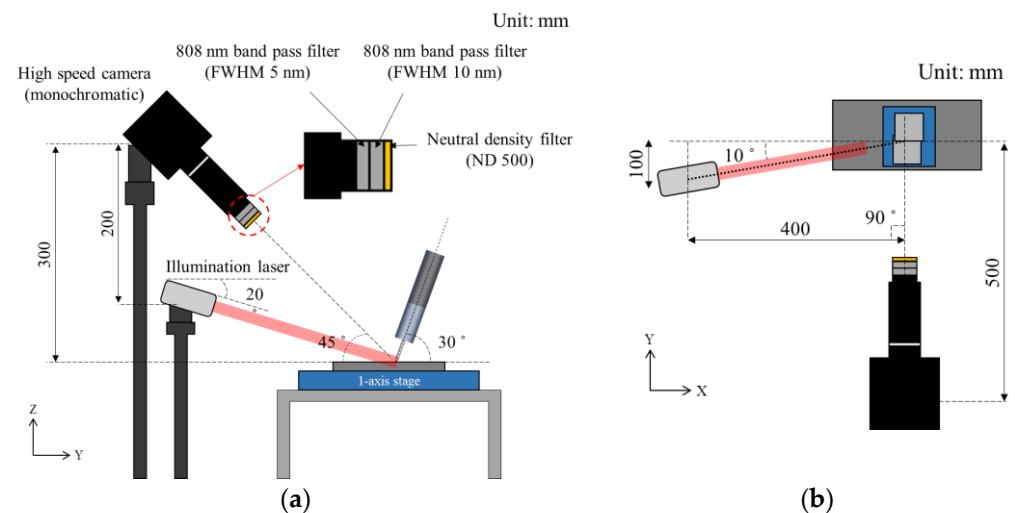|	Design Units				
Factor	−1.682	−1	0	1	1.682
X_1 (cm/min)	123	130	140	150	157
X_2 (m/min)	2.6	4.0	6.0	8.0	9.4
X_3 (m/min)	2.6	4.0	6.0	8.0	9.4

Figure 7. Schematic diagram of high-speed camera setup for recording the behavior of the molten pool: (**a**) Y-Z plane; (**b**) X-Y plane.
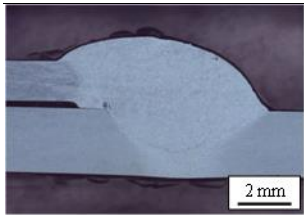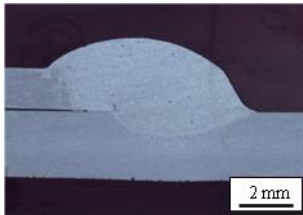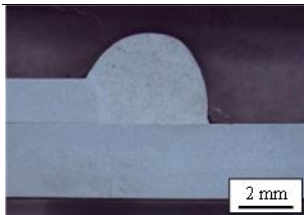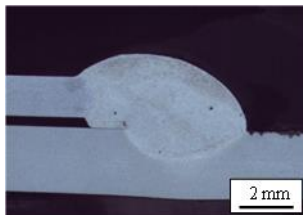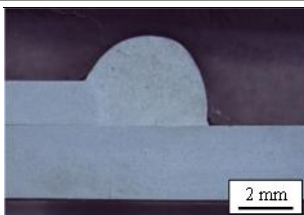
3. Results and Discussion
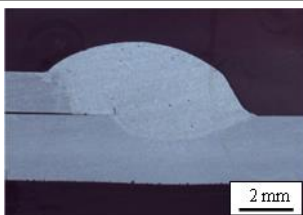
3.1. Effect of Welding Parameters on Bead Shape

Table 4 summarizes the experimental design matrix with the test results, that is, the measured response variables (Y_{leg}, Y_{pen}), according to the welding conditions. To observe the effects of each independent variable on the bead shape, macrographs of the weld cross-section at the six cubic points were compared. Table 5 lists the effect of each parameter on the actual weld shape after fixing two of the three parameters. X_2 and X_3 were fixed (X_2: 4 m/min, X_3: 8 m/min), and when the X_1 was increased, Y_{leg} decreased from 6.05 to 5.34 and Y_{pen} decreased from 1.97 to 1.05. X_1 and X_3 were fixed (X_1: 150 cm/min, X_3: 4 m/min), and when X_2 was increased, Y_{leg} increased from 3.52 to 4.81 and Y_{pen} increased from 0.00 to 1.16. In the case of X_3 under the test condition (X_1: 150 cm/min, X_2: 4 m/min), when X_3 was increased, Y_{leg} increased from 3.52 to 4.81, and Y_{pen} increased from 0.00 to 1.16. Figure 8 shows the main effect plots for Y_{leg} and Y_{pen}. Both Y_{leg} and Y_{pen} increased as X_1 decreased and X_2 and X_3 increased. Furthermore, X_2 and X_3 exhibited strong linearity with the response variables compared with X_1.

Table 4. Experimental design matrix.

Run	X_1	X_2	X_3	Y_{leg}			Y_{pen}		
1	−1	−1	−1	3.5	4.6	4.4	0.0	0.0	0.0
2	1	−1	−1	3.6	4.3	3.6	0.0	0.3	0.0
3	−1	1	−1	5.8	5.6	5.7	1.7	1.8	1.6
4	1	1	−1	5.0	5.2	5.0	1.3	1.3	1.3
5	−1	−1	1	6.0	6.2	6.2	2.0	1.7	1.8
6	1	−1	1	5.5	5.7	5.4	1.1	1.2	1.0
7	−1	1	1	7.5	7.6	7.6	4.8	5.0	5.0
8	1	1	1	7.7	6.7	7.4	4.0	4.3	4.3
9	−1.682	0	0	6.1	5.8	6.1	1.8	2.1	2.0
10	1.682	0	0	5.2	4.9	4.8	1.2	0.8	0.9
11	0	−1.682	0	3.8	5.0	4.1	0.0	0.3	0.2
12	0	1.682	0	7.4	7.0	7.5	4.0	4.1	3.9
13	0	0	−1.682	3.6	3.9	3.5	0.0	0.2	0.0
14	0	0	1.682	7.0	6.9	7.0	3.9	4.1	3.8
15	0	0	0	5.4	5.3	5.2	1.2	1.1	1.0
16	0	0	0	5.3	5.0	4.9	1.3	1.1	1.0
17	0	0	0	5.4	5.3	5.1	1.4	1.1	1.2
18	0	0	0	5.3	4.9	4.9	1.3	1.2	1.2
19	0	0	0	5.2	5.1	4.8	1.3	1.1	1.1
20	0	0	0	5.1	5.1	5.0	1.0	1.0	1.0

Table 5. Bead shape change according to welding parameters.

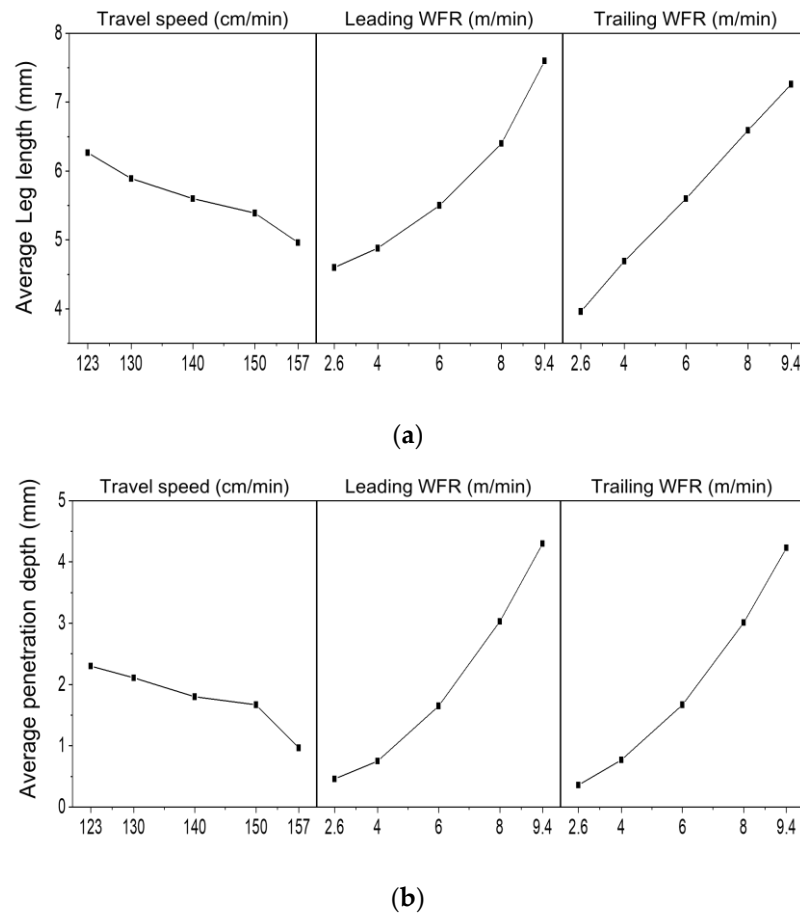| Parameter	Low Level	High Level
	Run 5	Run 6
X_1		
	Run 2	Run 4
X_2		
	Run 2	Run 6
X_3		

(a)

(b)

Figure 8. Main effects plots under welding conditions: (**a**) Y_{leg}; (**b**) Y_{pen}.

3.2. Model Estimation for Weld Bead Shape

3.2.1. Leg Length

RSM was applied to quantitatively explain the relationship between the welding parameters and bead shape. Table 6 summarizes the ANOVA results for Y_{leg}. The significance level (α) was set at 0.05. Therefore, the term with a *p*-value ≤ 0.05 was determined as a significant term. Because the *p*-values of the interaction and square terms $X_1 \times X_2$, $X_2 \times X_3$, $X_1 \times X_3$, and $X_1 \times X_2$ were over 0.05, respectively, these terms were determined to be insignificant and were excluded from the reduced model through backward elimination. In addition, F-value is an indicator for comparing sample groups and shows how far apart the mean sample group is between groups. Therefore, a high F-value means that it has a major influence on the independent variable. As a result of the ANOVA, the X_3 F-value was highest among the welding parameters. So, that means X_3 has a major influence on the Y_{leg}. The coefficient of determination (R^2) was 0.9414, indicating that the estimated model can predict 94.14% of the data.

$$Y_{leg} = 32.38 - 0.405X_1 - 0.334X_2 + 0.4814X_3 + 0.00135X_1^2 + 0.0617X_2^2 \qquad (1)$$

Table 6. ANOVA results of the reduced model for Y_{leg}.

Source	DF	Adj. SS	Adj. MS	F	p
Regression	5	71.40	14.28	173.37	0.00
Linear	3	68.18	22.73	275.91	0.00
X_1	1	3.07	3.07	37.26	0.00
X_2	1	27.12	27.12	329.31	0.00
X_3	1	37.96	37.96	461.17	0.00
Square	2	3.22	1.61	19.56	0.00
$X_1 \times X_1$	1	0.80	0.80	9.66	0.00
$X_2 \times X_2$	1	2.66	2.66	32.33	0.00
Residual error	54	4.45	0.08	-	-
Lack of fit	39	4.14	0.11	5.22	0.06
Pure error	15	0.31	0.02	-	-
R^2 = 0.9414	-	-	-	-	-
Adj R^2 = 0.9359	-	-	-	-	-

3.2.2. Penetration Depth

To analyze the penetration depth, the relationship between welding parameters and bead shape was quantitatively explained using RSM, identical to the analysis of leg length. Table 7 summarizes the analysis results for Y_{pen}. As a result of the ANOVA the X_2 F-value was highest among the welding parameter. So that mean X_2 has the major influence on the Y_{pen}. The p-value of all the terms were under the 0.05. The coefficient of determination (R^2) was 0.9924, indicating that the estimated model can predict 99.24% of the data.

$$
\begin{aligned}
Y_{pen} = \quad & 21.00 - 0.2835X_1 - 0.610X_2 + 0.059X_3 + 0.001146X_1^2 + 0.08315X_2^2 \\
& + 0.07578X_3^2 - 0.00312X_1X_3 - 0.00729X_1X_3 + 0.10313X_2X_3
\end{aligned}
\tag{2}
$$

Table 7. ANOVA results of the reduced model for Y_{pen}.

Source	DF	Adj. SS	Adj. MS	F	p
Regression	9	121.08	13.45	722.24	0.00
Linear	3	108.28	36.09	1937.66	0.00
X_1	1	2.61	2.61	140.24	0.00
X_2	1	53.10	53.10	2850.50	0.00
X_3	1	52.57	52.57	2822.24	0.00
Square	3	8.11	2.70	145.16	0.00
$X_1 \times X_1$	1	0.57	0.57	30.46	0.00
$X_2 \times X_2$	1	4.78	4.78	256.74	0.00
$X_3 \times X_3$	1	3.97	3.97	213.27	0.00
Interaction	3	4.69	1.56	83.89	0.00
$X_1 \times X_2$	1	0.09	0.09	5.03	0.03
$X_1 \times X_3$	1	0.51	0.51	27.40	0.00
$X_2 \times X_3$	1	4.08	4.08	219.24	0.00
Residual error	48	0.93	0.02	-	-
Lack of fit	33	0.77	0.02	2.02	0.07
Pure error	15	0.16	0.01	-	-
R^2 = 0.9924	-	-	-	-	-
Adj R^2 = 0.9910	-	-	-	-	-

3.3. Analysis of Phenomena through a High-Speed Camera

The effects of the welding parameters on the behaviors of the arc and molten pool were investigated based on the images acquired from the high-speed camera in Figure 7. Figure 9 shows high-speed images. The high-speed filming was performed with a bead on plate configuration, and the welding conditions were applied at 5 m/min for both X_2 and X_3. As shown in Figures 9 and 10, the leading arc directly strikes the solid-state base metal, which forms a narrow molten pool. Therefore, the leading arc had a direct effect on the penetration depth. The trailing arc is transferred to the molten pool created by the

leading arc, which expands the molten pool. Moreover, the solid surface induced by the leading arc force is filled with the molten metal generated by the trailing arc, the expansion of the molten pool remains stably maintained, and Y_{leg} increases [22]. A schematic of the behavior of the molten pool and arc is shown in Figure 10. The configuration of the lap fillet joint with the 2 mm thickness top plate and the 4 mm thickness bottom plate was used for high-speed filming. Table 8 shows the welding conditions, high-speed images, and cross-sections of the welding bead. WFR was fixed at 9.5 and 5.0 to observe the bead shape according to X_2 and X_3 when they have the same thermal energy. When the value of X_2 was higher than that of X_3, the Y_{leg} was 7.6 mm and the Y_{pen} was 3.0 mm. On the other hand, when X_3 was higher, the Y_{leg} was 8.0 mm and the Y_{pen} was 2.4 mm, that is, in the lap fillet joint as well, it was confirmed that the leading arc had an effect on the penetration depth formation, and the trailing arc had an effect on the leg length formation. When the value of X_2 was higher than that of X_3, a large number of porosities were observed in the weld metal. According to previous studies, porosities escape in the vertical direction [23]. When the penetration is deep, porosities become trapped because there is insufficient time to escape before solidification. In terms of material defects as well as weld bead geometry affected by process variables, the deformation of the material under the same heat input condition is less than that of single welding because the leading and trailing arcs are separated in tandem welding. Additionally, in the case of porosities, as mentioned above, the flow of the tandem molten pool is better than that of single arc welding, so trapped porosities are quickly released to the outside.
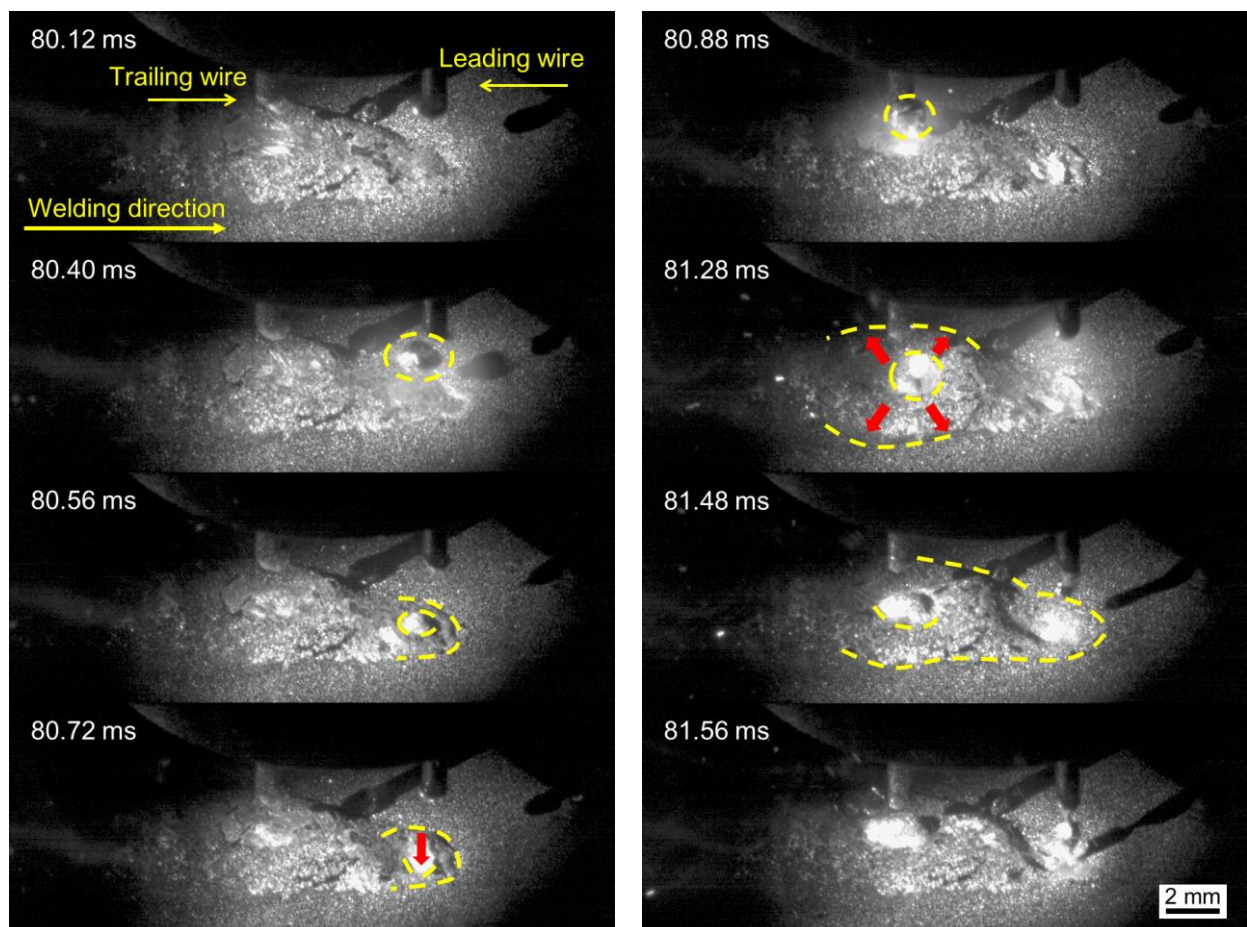

Figure 9. High-speed camera images of the molten pool when X_2 and X_3 are 5.0 m/min: behaviors of the leading arc and the molten pool at 80.72 ms; behaviors of the trailing arc and the molten pool at 81.28 ms.
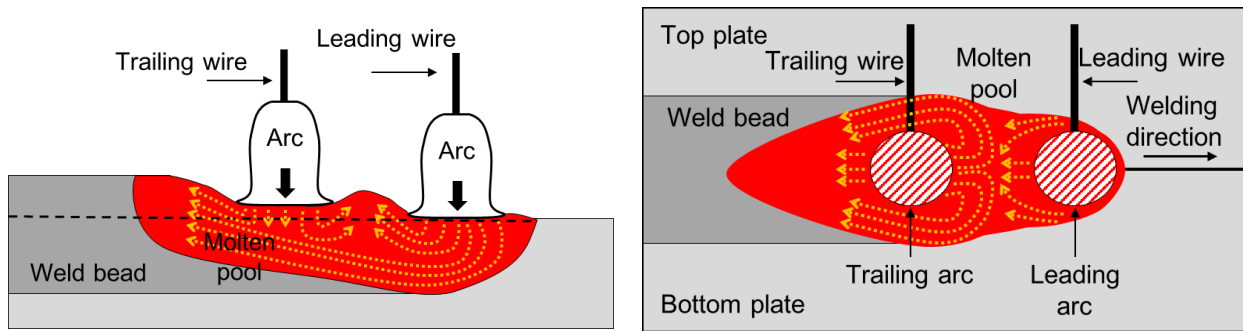
Figure 10. Schematic diagram of the molten pool convection in tandem gas metal arc welding.

Table 8. High-speed camera images of the molten pool and macrographs of the bead cross-section according to welding conditions.

Welding Condition	X_2 (m/min)	X_3 (m/min)	X_2 (m/min)	X_3 (m/min)
	9.5	5.0	5.0	9.5
High-speed camera images				
Cross-section				
Y_{leg} (mm)	7.6		8.0	
Y_{pen} (mm)	3.0		2.4	

3.4. Model-Based Optimization and Validation

Through this experiment, a regression model that can predict Y_{leg} and Y_{pen} was derived, and R^2 was 94% for Y_{leg} and 99% for Y_{pen}. Figure 11 shows contour plots of the response variables with respect to the independent variables. Y_{leg} and Y_{pen} decreased as X_1 increased within the range of X_1 (123–157 cm/min). As X_2 and X_3 increased, the response variables exhibited the same trend. Points 1–3 in Figure 11 are the test points for the estimation models. Table 9 lists the predicted and actual values at the test points. The test was repeated thrice. Consequently, in the case of point 1, the average deviations of Y_{leg} and Y_{pen} were 0.16 and 0.13 mm. For point 2, the average deviations of Y_{leg} and Y_{pen} were both 0.37 mm. Finally, at point 3, the average deviations of Y_{leg} and Y_{pen} were 0.37 and 0.23 mm.
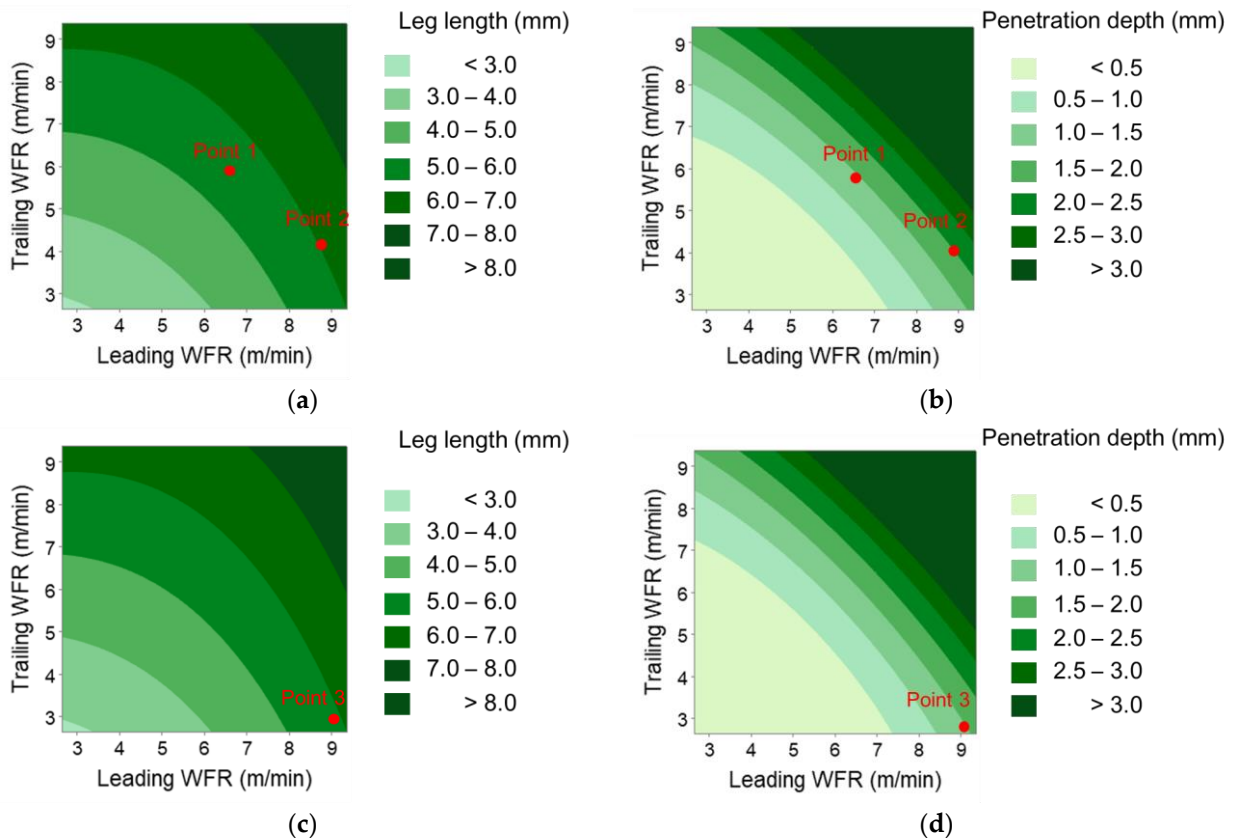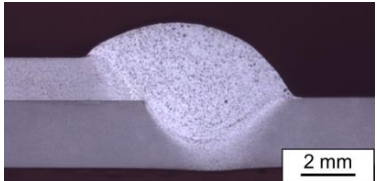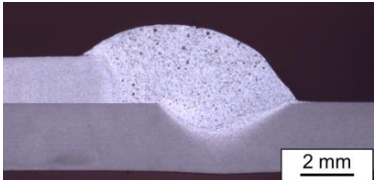

(a)

(b)

(c)

(d)

Figure 11. Contour plots for predicted Y_{leg} and Y_{pen}: (**a**) predicted Y_{leg} when X_1: 140 cm/min; (**b**) predicted Y_{pen} when X_1: 140 cm/min; (**c**) predicted Y_{leg} when X_1: 145 cm/min; (**d**) predicted Y_{pen} when X_1: 145 cm/min.

If the optimal welding conditions are determined based on the three points shown in Table 9, in terms of productivity, the condition of point 3 is considered an optimal condition because the welding speed is the fastest and the size of the weld also satisfies the required standard for the manufacturer.

Table 9. Validation conditions and results.

Point	Welding Parameter	Item	Value		Deviation		Cross-Section
			Y_{leg} (mm)	Y_{pen} (mm)	Y_{leg} (mm)	Y_{pen} (mm)	
1	(X_1) 140 cm/min; (X_2) 6.6 m/min; (X_3) 5.8 m/min	Predicted values	5.9	1.2			
		Actual value 1	6.0	1.4	0.1	0.2	
		Actual value 2	6.1	1.3	0.2	0.1	
		Actual value 3	6.1	1.3	0.2	0.1	
2	(X_1): 140 cm/min, (X_2): 8.7 m/min, (X_3): 4.1 m/min	Predicted values	6.0	1.9			
		Actual value 1	5.6	1.5	0.4	0.4	
		Actual value 2	5.6	1.5	0.4	0.4	
		Actual value 3	5.7	1.6	0.3	0.3	
3	(X_1): 145 cm/min, (X_2): 9.0 m/min, (X_3): 3.0 m/min	Predicted values	5.5	1.5			
		Actual value 1	5.2	1.1	0.3	0.1	
		Actual value 2	5.2	1.2	0.3	0.3	
		Actual value 3	5.1	1.2	0.4	0.3	

4. Conclusions

The effects of welding parameters (WS, leading WFR, and trailing WFR) on the bead shape (leg length and penetration depth) were investigated to predict and control the bead shape in tandem GMAW of aluminum 5083-O alloy. The following results and conclusions were obtained from this investigation:

1. The tandem GMAW process was used in these experiments, and a torch with a 7 mm gap between the tandem torches was designed and applied;
2. The bead shape (leg length and penetration depth) gradually decreased owing to the decrease in heat input as the WS increased within the WS range of 123–157 cm/min;
3. The leading arc directly strikes the solid to form a narrow molten article, which has an effect on the influence of the penetration depth;
4. The trailing arc is transferred to the molten pool created by the leading arc, which expanded the molten pool and influenced the leg length;
5. As a result of observing arc behavior using a high-speed camera, it was confirmed that the leading WFR affects the penetration depth, and the trailing WFR affects the leg length;
6. In the lap fillet joint tandem GMAW process using aluminum 5083-O alloy (thickness: 1.5 mm) for the top plate and aluminum 5083-O alloy (thickness: 2.5 mm) for the bottom plate, a regression equation was derived to predict the bead shape (leg length and penetration depth). The coefficient of determination (R^2) of the regression models was 0.9414 for the leg length and 0.9924 for the penetration depth;
7. It was validated that the estimated models were effective in predicting the weld bead shape of the aluminum 5083-O alloy single lap joint using the tandem GMAW process.

Author Contributions: Conceptualization, G.-G.K. and T.K.; methodology, T.K. and J.P.; formal analysis, G.-G.K. and D.-Y.K.; investigation, G.-G.K. and T.K.; writing—original draft preparation, G.-G.K. and T.K.; writing—review and editing, G.-G.K. and Y.-M.K.; supervision, Y.-M.K. and J.Y. All authors have read and agreed to the published version of the manuscript.

Institutional Review Board Statement: Not applicable.

Informed Consent Statement: Not applicable.

Data Availability Statement: Not applicable.

Conflicts of Interest: The authors declare no conflict of interest.

References

1. Fatchurrohman, N.; Iskandar, I.; Suraya, S.; Johan, K. Sustainable Analysis in the Product Development of Al-Metal Matrix Composites Automotive Component. *Appl. Mech. Mater.* **2015**, *695*, 32–35.
2. Srivyas, P.D.; Charoo, M. Application of Hybrid Aluminum Matrix Composite in Automotive Industry. *Mater. Today Proc.* **2019**, *18*, 3189–3200. [CrossRef]
3. Goecke, S.; Berlin, F.U.B.T.; Hedegård, J.; Joining, S.I.M.R.; ESAB Welding Equipment AB. Tandem mig/mag welding. *Weld. Rev. Publ. Esab* **2001**, *56*, 24–28.
4. Chen, D.; Chen, M.; Wu, C. Effects of phase difference on the behavior of arc and weld pool in tandem P-GMAW. *J. Mater. Process. Technol.* **2015**, *225*, 45–55. [CrossRef]
5. Wu, K.; Ding, N.; Yin, T.; Zeng, M.; Liang, Z. Effects of single and double pulses on microstructure and mechanical properties of weld joints during high-power double-wire GMAW. *J. Manuf. Process.* **2018**, *35*, 728–734. [CrossRef]
6. Zhang, L.; Su, S.; Wang, J.; Chen, S. Investigation of arc behaviour and metal transfer in cross arc welding. *J. Manuf. Process.* **2019**, *37*, 124–129. [CrossRef]
7. Rossini, L.F.S.; Reyes, R.A.V.; Spinelli, J.E. Double-wire tandem GMAW welding process of HSLA50 steel. *J. Manuf. Process.* **2019**, *45*, 227–233. [CrossRef]
8. Kolahan, F.; Heidari, M. A new approach for predicting and optimizing weld bead geometry in gmaw. *Int. J. Mech. Syst. Sci. Eng.* **2010**, *2*, 138–142.
9. Saravanan, S.; Pitchipoo, P. Optimization of GMAW Parameters to Improve the Mechanical Properties. *Appl. Mech. Mater.* **2015**, *813–814*, 456–461.
10. Jeyaganesh, D.; Ziout, A.; Qudeiri, J.A. Optimization of p-gmaw parameters using grey relational analysis and taguchi method. In Proceedings of the 2021 IEEE 12th International Conference on Mechanical and Intelligent Manufacturing Technologies (ICMIMT), Cape Town, South Africa, 13–15 May 2021; pp. 191–196.
11. Venkadeshwaran, P.; Sakthivel, R.; Sridevi, R.; Meeran, R.A.; Chandrasekaran, K. Optimization of welding parameter on aa2014 in gmaw. *Int. J. Emerg. Technol. Innov. Eng.* **2015**, *1*, 60–66.
12. Ramarao, M.; King, M.F.L.; Sivakumar, A.; Manikandan, V.; Vijayakumar, M.; Subbiah, R. Optimizing GMAW parameters to achieve high impact strength of the dissimilar weld joints using Taguchi approach. *Mater. Today Proc.* **2022**, *50*, 861–866. [CrossRef]
13. Duan, B.; Wang, J.C.; Lu, Z.H.; Zhang, G.X.; Zhang, C.H. Parameter Analysis and Optimization of the Rotating Arc NG-GMAW Welding Process. *Int. J. Simul. Model.* **2018**, *17*, 170–179. [CrossRef]
14. Tham, G.; Yaakub, M.Y.; Abas, S.K.; Manurung, Y.H.; Abu Jalil, B. Predicting the GMAW 3F T-Fillet Geometry and Its Welding Parameter. *Procedia Eng.* **2012**, *41*, 1794–1799. [CrossRef]
15. Yu, J.; Kim, D. Effects of welding current and torch position parameters on minimizing the weld porosity of zinc-coated steel. *Int. J. Adv. Manuf. Technol.* **2017**, *95*, 551–567. [CrossRef]
16. Shen, X.; Ma, G.; Chen, P. Effect of welding process parameters on hybrid GMAW-GTAW welding process of AZ31B magnesium alloy. *Int. J. Adv. Manuf. Technol.* **2018**, *94*, 2811–2819. [CrossRef]
17. Rodríguez-Hernández, T.; Cruz-Hernández, V.; García-Rentería, M.; Torres-Gonzalez, R.; García-Villarreal, S.; Curiel-López, F.; Falcón-Franco, L. First assessment on the microstructure and mechanical properties of gtaw-gmaw hybrid welding of 6061-t6 aa. *J. Manuf. Process.* **2020**, *59*, 658–667. [CrossRef]
18. Lee, D.Y.; Leifsson, L.; Kim, J.-Y.; Lee, S.H. Optimisation of hybrid tandem metal active gas welding using Gaussian process regression. *Sci. Technol. Weld. Join.* **2020**, *25*, 208–217. [CrossRef]
19. Wu, D.; Hua, X.; Ye, D.; Ma, X.; Li, F. Understanding of the weld pool convection in twin-wire GMAW process. *Int. J. Adv. Manuf. Technol.* **2017**, *88*, 219–227. [CrossRef]
20. Häßler, M.; Rose, S.; Füssel, U. The influence of arc interactions and a central filler wire on shielding gas flow in tandem GMAW. *Weld. World* **2016**, *60*, 713–718. [CrossRef]
21. Wu, K.; Wang, Y.; Tao, T.; Zhan, J.; Hong, X. Effect of phase shift on arc interference and weld bead formation in aluminum alloy tandem GMAW with a median pulsed waveform. *Int. J. Adv. Manuf. Technol.* **2022**, *120*, 8013–8030. [CrossRef]

22. Ueyama, T.; Ohnawa, T.; Tanaka, M.; Nakata, K. Effects of torch configuration and welding current on weld bead formation in high speed tandem pulsed gas metal arc welding of steel sheets. *Sci. Technol. Weld. Join.* **2005**, *10*, 750–759. [CrossRef]

23. Ahsan, R.U.; Kim, Y.R.; Kim, C.H.; Kim, J.W.; Ashiri, R.; Park, Y.D. Porosity formation mechanisms in cold metal transfer (CMT) gas metal arc welding (GMAW) of zinc coated steels. *Sci. Technol. Weld. Join.* **2016**, *21*, 209–215. [CrossRef]